Exploration of alloy 441 chemistry for solid oxide fuel cell interconnect application

Paul D. Jablonski [a],[*],[1], Christopher J. Cowen [a], John S. Sears [a],[b]

[a] National Energy Technology Laboratory, United States Department of Energy, 1450 Queen Ave., SW, Albany, OR 97321, United States
[b] Parsons/RDS, Post Office Box 618, South Park, PA 15129, United States

ABSTRACT

Alloy 441 stainless steel (UNS S 44100) is being considered for application as an SOFC interconnect material. There are several advantages to the selection of this alloy over other iron-based or nickel-based alloys: first and foremost alloy 441ss is a production alloy which is both low in cost and readily available. Second, the coefficient of thermal expansion (CTE) more closely matches the CTE of the adjoining ceramic components of the fuel cell. Third, this alloy forms the Laves phase at typical SOFC operating temperatures of 600–800 °C. It is thought that the Laves phase preferentially consumes the Si present in the alloy microstructure. As a result it has been postulated that the long-term area specific resistance (ASR) performance degradation often seen with other ferritic stainless steels, which is associated with the formation of electrically resistive Si-rich oxide subscales, may be avoidable with alloy 441ss. In this paper we explore the physical metallurgy of alloy 441, combining computational thermodynamics with experimental verification, and discuss the results with regards to Laves phase formation under SOFC operating conditions. We show that the incorporation of the Laves phase into the microstructure cannot in itself remove sufficient Si from the ferritic matrix in order to completely avoid the formation of Si-rich oxide subscales. However, the thickness, morphology, and continuity of the Si-rich subscale that forms in this alloy is modified in comparison to non-Laves forming ferritic stainless steel alloys and therefore may not be as detrimental to long-term SOFC performance.

Published by Elsevier B.V.

1. Introduction

Solid oxide fuel cells (SOFC) are solid state energy conversion devices [1,2] that convert a fuel, such as H$_2$ or CO, directly into electricity without combustion. In their simplest form they consist of an anode, a cathode, and an electrolyte. A single cell can produce current density and voltage on the order of 1 A cm^{-2} and 1 V, respectively. In order to develop greater power output, multiple cells are grouped together. In planar SOFC they are simply stacked together with an "interconnect" separating each cell [2,3]. The interconnect acts as an air/fuel separator and is also part of the electrical circuit.

The core goal of the Solid State Energy Conversion Alliance (SECA) is the development of SOFCs that meet performance goals with a factory production cost of \$400/kwh or less [4–6]. One of the most cost enabling developments made over the past few years is the development of oxide component materials capable of operating at lower temperatures in the range of 700–800 °C [7–12]. This lower operating temperature has provided room for

the consideration of metallic materials to be used for interconnect applications [12–18]. Metallic interconnects have several advantages over ceramic materials: low cost, high ease in manufacturing, and high electrical conductivity. Most metals and alloys will oxidize under both the anodic and cathodic conditions present within a SOFC, thus a chief requirement for a metal interconnect is that the base metal oxide scale must be electrically conductive since the interconnect is part of the electrical circuit. Common high temperature metallic alloys form oxide scales that contain Cr, Si, and Al oxides, among others. Under SOFC operating conditions chromia is an intrinsic semiconductor while both silica and alumina are strong insulators. Therefore, alloys that preferentially form chromia-based oxide scales are desirable candidates to be used as SOFC interconnects.

Many SOFC designs will operate at temperatures exceeding 700 °C. At these temperatures in the moist SOFC cathode environment, chrome-containing species evaporate and the Cr from these compounds deposits on electrochemically active sites at the cathode–electrolyte interface. This degrades the electrical performance of the SOFC because the presence of Cr poisons the necessary electrochemical reactions that take place in the cathode [19–25]. The formation of a Cr–Mn spinel outer layer on top of a chromia subscale will reduce but will not eliminate Cr evaporation, and thus

* Corresponding author. Tel.: +1 541 967 5982; fax: +1 541 967 5958.
E-mail address: Paul.Jablonski@netl.doe.gov (P.D. Jablonski).
[1] www.netl.doe.gov.

it will not prevent the Cr from poisoning the electrochemical reactions. Consequently, there has been considerable attention placed on developing coatings to prevent Cr migration from the stainless steel interconnects into the cathode [25–29].

Several commercial alloys have been developed for SOFC interconnect applications such as Crofer 22 APU (ThyssenKrupp VDM), Hitachi ZMG 232 (Hitachi Metals), and Ebrite (Allegheny Ludlum) which all form chromium-rich oxide scales under oxidizing conditions. One disadvantage of these alloys is that they are considered "specialty" alloys, due to the addition of rare earth elements and/or extra processing steps to lower Al and Si contents, and may not be as inexpensive or readily available as other ferritic stainless steels. Additionally, it has been observed that even with special processing, these alloys can contain sufficient Si to form at least a semi-continuous Si-rich subscale [30]. Several authors [31–33] have reported that alloy 441ss can be utilized as an interconnect with good results, even though this alloy may nominally contain up to 1 weight percent (wt.%) Si [34] and still remain within the 441ss chemistry specification. Besides the usual Cr and Mn, this alloy also contains Nb and Ti and is known to form the Laves phase, a Fe_2Nb-based intermetallic phase with a C14 hexagonal crystal structure [35,36]. Previous research has shown that Si has preferentially partitioned to this phase over the ferritic matrix [33,37–39]. The Laves phase has also been observed to reside on ferritic grain boundaries [33,39–40] and has been suggested to be a blocking agent for grain boundary diffusion [41]. The present work explores both of these theories by evaluating the oxidation resistance of conventional 441ss, henceforth designated 441ss – std, as well as an analogous alloy, henceforth designated 441ss – Nb (interpret as "441ss minus Niobium"), that does not form the Laves phase because it does not contain Nb. Finally, the Laves phase stability for alloy 441 is explored as a function of allowable "in-spec" nominal alloy chemistry and temperature.

2. Experimental techniques

2.1. Alloy design and manufacture

Experimental alloy design was first evaluated theoretically with the use of Thermo-Calc Software (version s) utilizing the TcFe6 database. High purity starting materials were used to formulate the 441ss – std and 441ss – Nb alloys shown in Table 1. Approximately 6800 g of high purity raw materials were formed into compacts prior to melting. Each alloy was induction melted under inert gas and poured into a 75 mm cylindrical graphite mold. After casting, the hot-tops of each ingot were removed with a band saw, and a 2 mm thick slice was taken from each ingot for chemical analysis. The metal chemistries were determined by XRF with a Rigaku ZSX Primus II utilizing NIST traceable standards (reported values are accurate to 0.01 wt.%); carbon chemistries were determined with a LECO CS444LS using NIST certified standards (reported values are accurate to 0.002 wt.%). The sidewalls of the ingots were conditioned on a lathe, and each ingot was given a computationally optimized homogenization heat treatment utilizing the method described in [42]. The homogenized ingots were bagged in protective stainless steel foil pouches and preheated at 900 °C for 3 h prior to fabrication. Hot working consisted of forging and rolling to fabricate the round ingots into slab shapes, which were ultimately formed into strip product. These strips were hot worked to a thickness of approximately 3 mm. Subsequently, these strips were conditioned to remove oxidation products and any residual surface defects prior to cold rolling. Each alloy was subsequently cold rolled to approximately 1 mm thickness.

Table 1
Experimental alloy chemistry aims and measured chemistries are shown in italics below. The metal chemistries were determined by XRF with a Rigaku ZSX Primus II utilizing NIST traceable standards (reported values are accurate to 0.01 wt.%); carbon chemistries were determined with a LECO CS444LS using NIST certified standards (reported values are accurate to 0.002 wt.%).

Designation	Fe	Cr	C	Mn	Si	Nb	Ti
441ss – std	Bal	18	0.009	0.35	0.34	0.5	0.22
		18.1	*0.01*	*0.34*	*0.33*	*0.5*	*0.22*
441ss – Nb	Bal	18	0.009	0.35	0.34	0	0.22
		18.1	*0.01*	*0.34*	*0.34*	*0*	*0.21*

2.2. Alloy testing and evaluation

Oxidation test coupons were cut from the cold worked strip of each of the alloys with dimensions of approximately 12 mm × 24 mm × sheet thickness. The coupons were polished to a 600-grit surface finish before exposure. Prior to oxidation testing the starting weights and physical dimensions of the coupons were measured and recorded. Isothermal oxidation tests were conducted at 800 °C in laboratory air. After a predetermined time interval, the time-increment coupon was removed from the heated furnace to cool and the weight of the coupon was measured and recorded. In this way, individual coupons represent each time increment. Likewise, isochronal oxidation tests were conducted in the range of 650–850 °C for 100 h in laboratory air. Oxide scale surfaces were examined by scanning electron microscopy (SEM) techniques. Chemistries of the oxidized surfaces were determined by energy dispersive X-ray analysis (EDX). Oxidized coupons were then sectioned and polished via conventional metallographic procedures to view the scales in a cross-sectional orientation. Care was taken to avoid induced surface Si contamination from silica polishing media by only using submicron alumina or diamond for the final polishing steps. The cross sections were analyzed by SEM with a combination of EDX and wavelength dispersive X-ray analysis (WDX) using in situ standards for metal and oxide scale chemistry.

To determine the Laves phase solvus, samples of both alloys were solution heat treated at 1200 °C for 1 h followed by water quenching to ensure that the Laves phase was fully dissolved within the microstructure. Subsequently, samples were annealed for 1 h at temperatures ranging from 800 °C to 1100 °C followed by water quenching. Portions of these coupons were cross sectioned and examined in the SEM in order to estimate the Laves solvus temperature and to obtain images used to calculate the volume fraction of Laves phase using the image analysis software Image J. Six to eight images were examined from each condition in order to achieve a level of statistical confidence in the measured values.

Select samples were prepared for transmission electron microscopy (TEM) examination using the Helios Nano Lab Dual Beam-Focused Ion Beam (DB-FIB) system. Specifically, this allowed for sample preparation and review within the critical alloy/oxide scale region. The samples were then examined in a Philips/FEI CM200 TEM. The chemistries of select areas of interest were determined by EDX in the TEM.

3. Results

3.1. Experimental alloy chemistry

The targeted and measured chemistries of the 441ss – std and 441ss – Nb alloys produced in this study are shown in Table 1. It is apparent from Table 1 that the only chemical difference between the two alloys in this study is the lack of Nb in the 441ss – Nb alloy. As mentioned earlier, the Nb was not included in the 441ss – Nb alloy in order to prevent the formation of the Laves phase; this
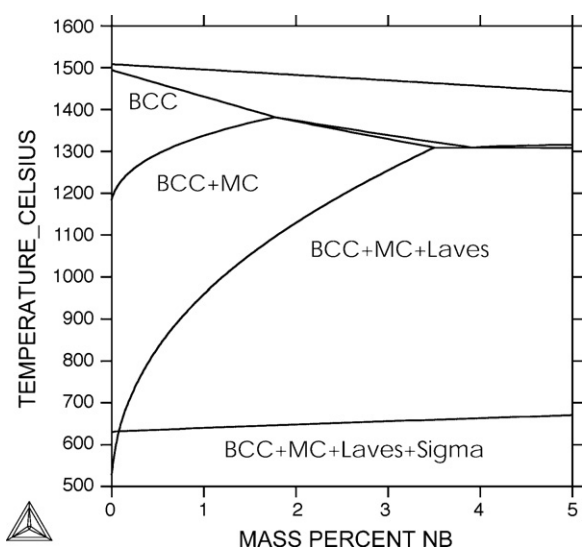
Fig. 1. A vertical section through the alloy 441ss phase diagram as a function of Nb content calculated with Thermo-Calc Software (version s) utilizing the TcFe6 database is shown above. Note that the Laves solvus ranged from less than 600 °C at 0 wt.% Nb to 1300 °C at about 3 wt.% Nb (which is well above the specification maximum of 0.9 wt.%). The other alloying elements were set to that of the nominal 441ss alloy composition (Table 1).
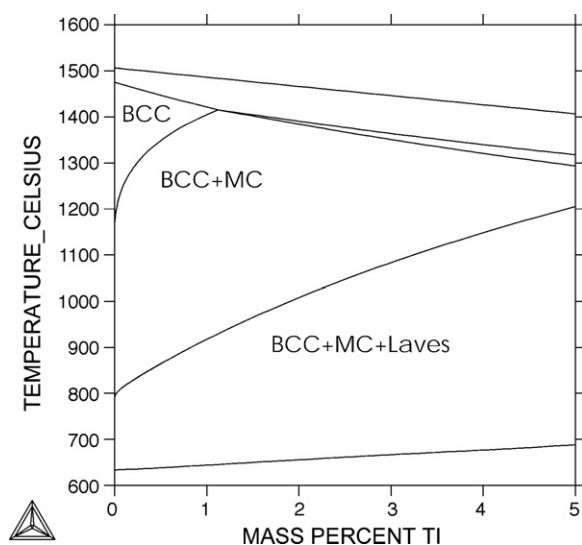

Fig. 2. A vertical section through the alloy 441ss phase diagram as a function of Ti content calculated with Thermo-Calc Software (version s) utilizing the TcFe6 is shown above. Note that the Laves solvus ranged from less than 800 °C at 0 wt.% Ti to 1200 °C at about 5 wt.% Ti (which is well above the specification maximum of 0.5 wt.%). The other alloying elements were set to that of the nominal 441ss alloy composition (Table 1).

allowed a direct evaluation of the effectiveness of the Laves phase in gettering Si from the ferritic matrix, as well as an evaluation of the formation of Si-rich oxide subscales in both the presence and absence of the Laves phase within the microstructure. Since alloy 441ss is a production alloy, both the Si and Mn contents must remain below a maximum amount of 1 wt.% for the alloy to remain within specification. The Si content for the alloys in this study was targeted at 0.34 wt.%, and the target was met due to the purity of the starting raw materials. When this alloy is produced in tonnage quantities in a production environment, the starting raw materials include various forms of recycled steel, which can make maintaining Si contents significantly below the maximum of 1 wt.% difficult to impossible without the utilization of specialized melting techniques such as vacuum remelting. The potential effects of such variations in alloy composition on interconnect performance, while still within the specification range for alloy 441ss, are discussed subsequently.

3.2. Effect of chemistry on Laves solvus within the range of alloy 441

Not surprisingly, Nb stabilizes the Laves phase more than any other alloying element in alloy 441ss. Fig. 1 shows a vertical section through the alloy 441ss phase diagram as a function of Nb content. Note that the Laves solvus ranges from less than 600 °C at 0 wt.% Nb to 1300 °C at about 3 wt.% Nb (which is well above the specification maximum of 0.9 wt.%); the salient point here is the steep rise of the Laves solvus line as a function of wt.% Nb. The other alloying elements were set to that of the 441ss − std alloy which is the nominal alloy 441ss composition (Table 1). Titanium is the second most effective Laves phase stabilizer in this alloy. Fig. 2 shows a vertical section through the alloy 441ss phase diagram as a function of Ti content. Note that the Laves solvus ranges from less than 800 °C at 0 wt.% Ti to 1200 °C at about 5 wt.% Ti (which again is well above the specification maximum of 0.5 wt.%). As was done in the previous calculation, the other alloying elements were set to that of the 441ss − std alloy which is the nominal alloy 441ss composition (including 0.5 wt.% Nb, which explains the high Laves solvus with 0 wt.% Ti). Note that the Laves solvus line rises more steeply with

Nb compared to Ti additions. In comparison to Nb or Ti, C has the opposite effect, reducing the Laves phase stability, likely because it competes for the Nb and Ti in the alloy to form carbides rather than the Fe_2Nb-based Laves phase. At 0 wt.% carbon, the Laves solvus is approximately 840 °C. With increasing C content the Laves solvus decreases linearly to about 775 °C at 0.03 wt.% C, the specification maximum. Thus, the amount and stability of Laves phase is expected to be dependent upon alloy chemistry. The Thermo-Calc determined Laves phase solvus for the 441ss − std alloy (Table 1), which is the nominal alloy 441ss chemistry, is approximately 833 °C. Likewise, considering the alloy 441ss chemistry with low Nb (0.39 wt.%) and Ti (0.1 wt.%) and high C (0.01 wt.%)—all values still within the alloy 441ss specification—predicts a Laves phase solvus of 766 °C which is below the nominal SOFC operating temperature. Similar results were obtained regardless of which thermodynamic database was considered, including the TcFe3, TcFe5, TcFe6, SSUB4, Fe, and Ni databases. Thus, if the presence of Laves phase is critical to the interconnect performance, the alloy 441ss nominal chemistry and SOFC operating temperature will both be important parameters to consider in order to produce and maintain the appropriate alloy microstructure.

3.3. Silicon in the laves phase

If the amount of Si in the alloy is known and assumed to all report to the Laves phase, the amount of Si in the Laves phase (W_{Si_Laves}) can be calculated by:

$$W_{Si\_Laves} = \frac{W_{Si\_Alloy}((1 - V_{MC} - V_{Laves})\rho_{BCC} + V_{Laves}\rho_{Laves} + V_{MC}\rho_{MC})}{V_{Laves}\rho_{Laves}}$$

(1)

which depends on the volume fraction and the densities of the phases contained within the alloy, as well as the overall Si content (W_{Si_Alloy}). Since the amount of MC carbide predicted is very low in this alloy (<0.1 vol.%), terms multiplied by V_{MC} could be dropped to simplify the expression; however, we include them in our calculations for completeness. The mass and volume fractions of each phase, along with the total system volume and mass, can be calculated with Thermo-Calc, and from these values the densities of

Table 2
Physical quantities of the 441 – std alloy calculated with Thermo-Calc using the TcFe6 database are shown in bold below. The remaining values were derived from these Thermo-Calc values. The table thus provided the constants which were used in evaluating Eq. (1).

Designation	Overall alloy	BCC	Laves	MC
Volume fraction phase	1	**0.997**	**2.11(10)$^{-3}$**	**8.57(10)$^{-4}$**
Volume (cm^3)	**7.35**	7.33	1.56(10)$^{-2}$	6.30(10)$^{-3}$
Mass (g)	**54.0**	57.8	**1.25(10)$^{-1}$**	**3.76(10)$^{-2}$**
Density (g/cm^3)	7.48	7.48	8.05	5.96

each of the phases can be calculated (Table 2). Thus, the expected Laves phase chemistry with respect to Si can be calculated for the 441ss – std alloy based upon the measured volume fraction of Laves phase and the overall Si content. Experimentally, about 3.1 wt.% Si was measured locally by WDX in the Laves phase found in the 441ss – std alloy. The volume percent of Laves phase measured was ~1.75% after aging at 800 °C for 1 h followed by water quenching. These measurements, along with the predictive curve for a 0.34-wt.% Si containing alloy based on Eq. (1), are plotted in Fig. 3. It is readily apparent that the two measured values intersect the predictive curve in vastly different locations. These differences are well outside of any reasonable experimental error, and thus the conclusion is that the Laves phase does not contain all of the Si within the alloy. The estimated residual Si content in the ferritic matrix is 0.23 wt.%, based on the measured Si content in the Laves phase and volume percent of Laves phase. Therefore, for a nominal Si content of 0.34 wt.%, a significant amount of Si remains available to potentially diffuse through the ferritic matrix and contribute to the formation of a Si-rich oxide subscale when/if it reaches the alloy/oxide interface.

3.4. Laves solvus temperature

Fig. 4 shows a plot of the experimentally determined Laves phase volume fraction as a function of aging temperature. All the samples in Fig. 4 were solutioned for 1 h at 1200 °C and water quenched prior to aging to put all the Laves phase into solution. The amount of Laves phase that precipitated during aging was observed to decrease monotonically from 800 °C to 1000 °C. The Laves phase was observed to reside on grain boundaries and within grain inte-
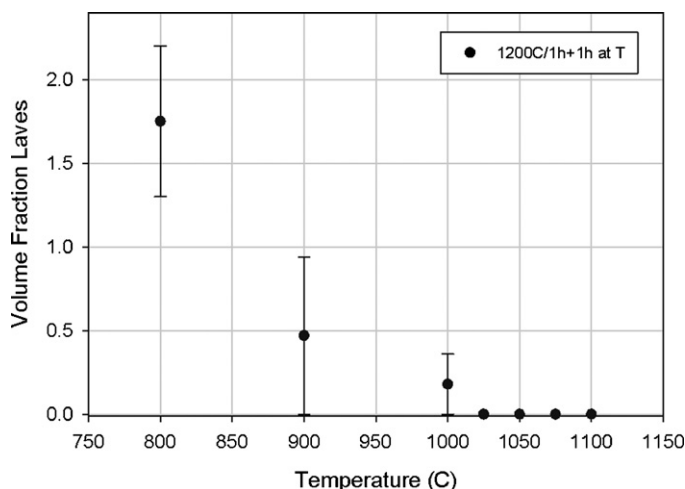

Fig. 4. The experimentally determined Laves phase volume fraction as a function of temperature is shown above. The error bars shown at each point represent one standard deviation. A total of 6–8 areas were evaluated for each condition.

riors at all aging temperatures below 1025 °C. At temperatures of 1025 °C and above, no Laves phase was observed.

3.5. Isochronal oxidation and rate constant

Fig. 5 shows the 100 h specific mass gain results as a function of exposure temperature. Under these short-term test conditions, the 441ss – Nb alloy, which is free of the Laves phase, exhibits a higher specific mass gain at nearly all test temperatures. The exception is the 650 °C test in which the 441ss – std alloy exhibits nearly zero specific mass gain while the 441 – Nb alloy exhibits zero mass gain. It is likely this difference is within experimental error. Furthermore, this result does not mean that the 441ss – Nb specimen does not oxidize at 650 °C, since it clearly exhibits discoloration after exposure. Fig. 6 shows the oxidation rate constant as a function of inverse temperature for each of the alloys. The oxidation rate constant increases nearly linearly with increasing temperature. Once again, the 441ss – Nb alloy exhibits the higher value at all temperatures.
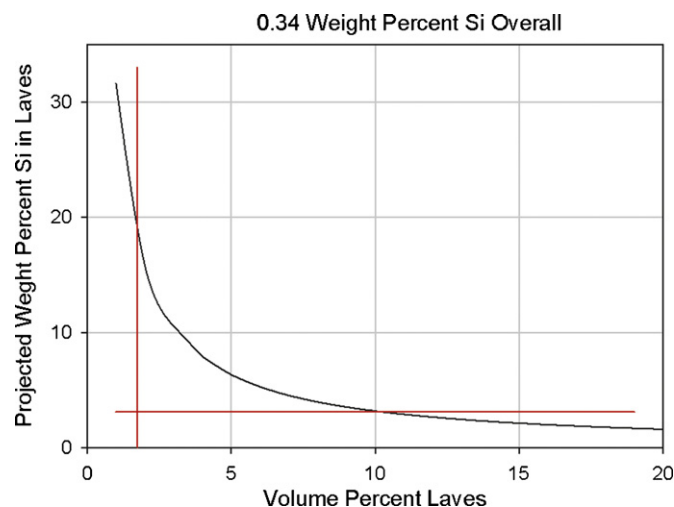

Fig. 3. The weight percent Si in the Laves phase is plotted as a function of volume percent Laves phase in the diagram above. The vertical line is drawn at the measured volume percent Laves value (1.75%) and the horizontal line is drawn at the measured wt% Si in the Laves (3.1%). Note that the intersection of the horizontal and vertical lines is well away from the curve based on Eq. (1) which indicates that not all of the Si is reporting to the Laves phase for an alloy with 0.34 wt.% Si overall.
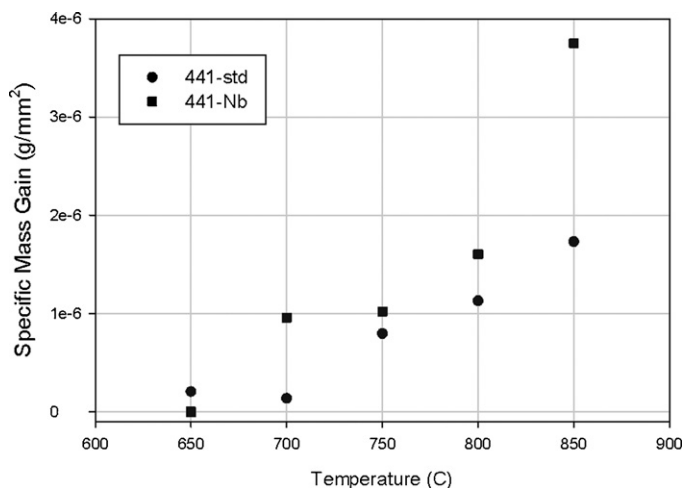

Fig. 5. Isochronal specific mass gain as a function of exposure temperature is shown above. Time at temperature: 100 h.
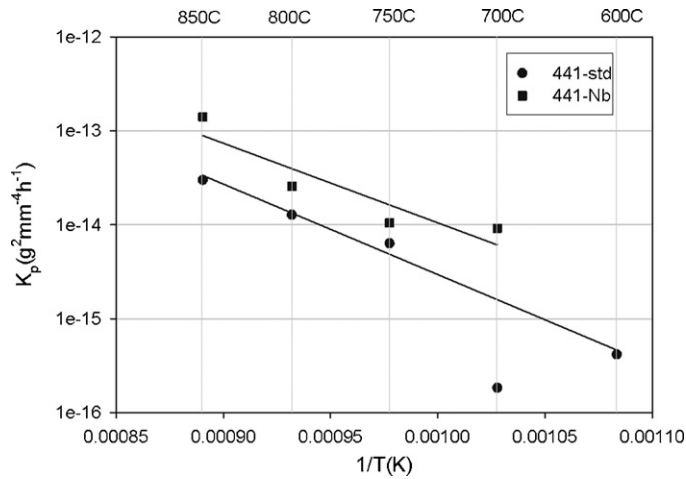
Fig. 6. The oxidation rate constants as a function of inverse exposure temperature is shown above. Time at temperature: 100 h. 441ss − std: $K_p = -4.9 - 9630T^{-1}$. 441ss − Nb: $K_p = -5.5 - 8470T^{-1}$. K_p ($g^2\ mm^{-4}\ h^{-1}$). T (K).
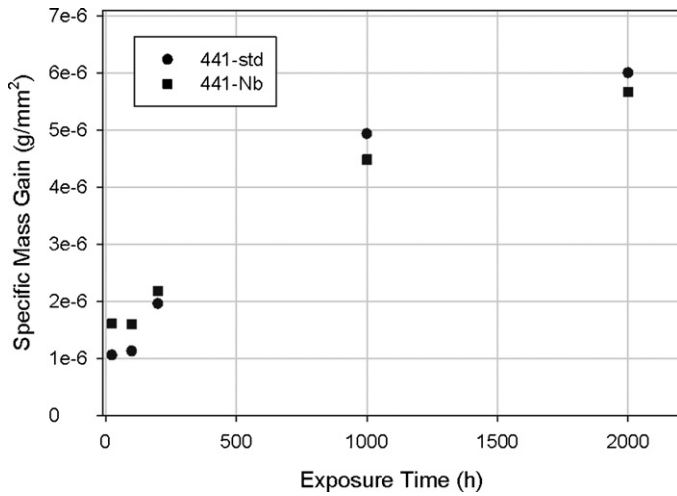

Fig. 7. Specific mass gain at 800 °C as a function of exposure time is shown above.

3.6. Isothermal oxidation

Fig. 7 shows the specific mass gain at 800 °C as a function of time for both alloys. At times up to 200 h the 441ss − Nb alloy exhibits
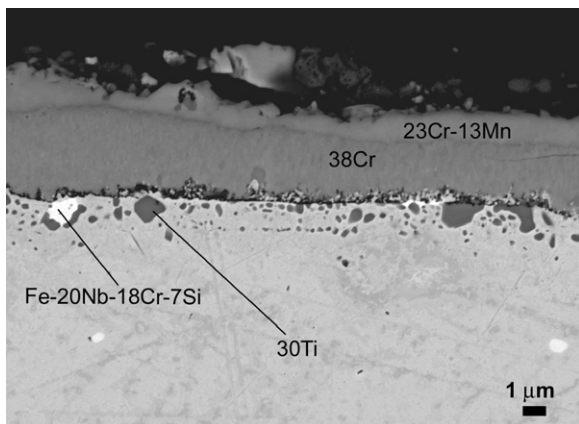

Fig. 8. SEM cross section at the base metal/scale interface for alloy 441ss − std exposed for 2000 h at 800 °C is shown above. Note that the values are given in at.% and the balance is oxygen (with the exception of Laves phase which has a balance of Fe as shown).
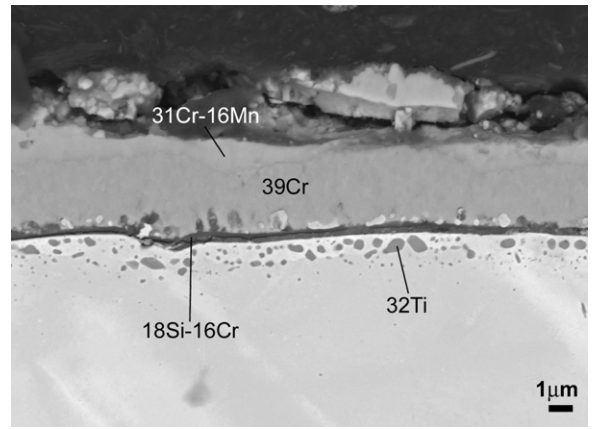

Fig. 9. SEM cross section at the base metal/scale interface for alloy 441ss − Nb exposed for 2000 h at 800 °C is shown above. Note that the values are given in at.% and the balance is oxygen.

the higher specific mass gain, in agreement with the isochronal results. However, at the 1000 and 2000 h times, the 441ss − std alloy exhibits the higher specific mass gain. Fig. 8 shows a cross section through the scale for the 441ss − std alloy after 2000 h exposure at 800 °C. The scale is duplex in nature, with a Cr–Mn-rich outer scale and essentially a pure chromia inner scale. Titanium-rich internal oxidation is observed within the base metal below the chromia scale. Occasionally the Laves phase is observed near the scale/metal interface as well, but these particles do not appear to oxidize at a different rate than the surrounding matrix. Many of the major features of the scale on the 441ss − Nb alloy after 2000 h of exposure appear similar (Fig. 9). The outer scale is Cr–Mn-rich and the inner scale is essentially a pure Cr oxide. Titanium-rich internal oxidation is also observed within the base metal just below the scale. However, a continuous layer of Si-rich oxide, measuring approximately 0.3–0.4 μm in thickness, is observed at the scale–metal interface of the 441ss − Nb alloy. This Si-rich layer is apparent on all the cross sections of the 441ss − Nb alloy, even after only 24 h of oxidation (although it appears thinner with shorter exposure time). Closer examination of the 441ss − std scale also reveals regions which are Si-rich (Fig. 10), however these regions are not continuous, nor are they as thick as those observed within the 441ss − Nb alloy. Note that the excitation voltage used for these chemistry measurements was 10 kV, which provides better spatial resolution for such analy-
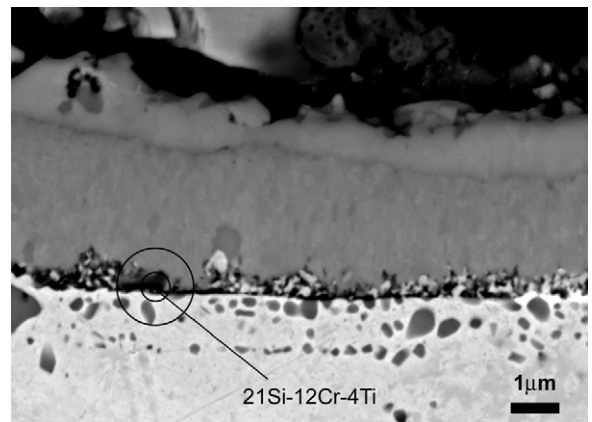

Fig. 10. SEM cross section at the base metal/scale interface for alloy 441ss − std is shown above. Note that the values given are an average of three similar areas and are in at.% with the balance being oxygen. The circles indicate the interaction area for two excitation voltages: 10 kV (inner, used in the analysis) and 20 kV (outer, commonly used by other researchers).
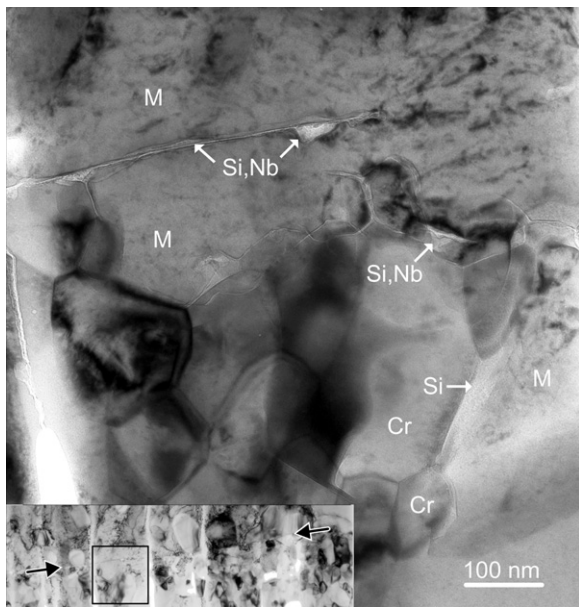
Fig. 11. A low magnification BF TEM image of the foil is shown in the inset. The scale/metal interface appears linear (indicated by the arrows). Note that the broad, nearly vertical linears are due to thinning. A higher magnification image of the indicated area (box) revealed an amorphous Si-rich layer at the scale/metal interface. This layer also encapsulated several chromia grains within the first 250 nm of the scale. The width of the Si-rich layer in both regions is approximately 10 nm. The various indicated areas are M = metal matrix, Cr = chrome rich oxide, Si = silicon rich oxide, and Si,Nb = silicon rich oxide with some Nb.

ses. Fig. 10 also shows two circles superimposed on the SEM image, which indicate the estimated areas of the sample from which X-rays are excited by 10 kV and 20 kV beams, respectively. The 10 kV beam better samples this Si-rich area while the 20 kV beam over samples into the matrix and Cr-rich oxide scale.

3.7. Transmission electron microscopy

A representative bright field (BF) TEM image of the scale/metal interface in the 441ss − std alloy is shown in Fig. 11. The inset shows a low magnification BF TEM image of the foil. Even at low magnification, the scale/metal interface is readily apparent. Examination at higher magnification confirms the presence of an amorphous Si-rich layer at the scale/metal interface. This layer also encapsulates several chromia grains within the first 250 nm of the scale. The width of the silica layer in all regions is approximately 10 nm.

4. Discussion

It is very clear that without the addition of Nb, alloy 441ss readily forms a relatively thick Si-rich oxide scale at the base metal/oxide interface (compare Figs. 8 and 9). The reason for this difference is less apparent. Horita et al. [41] have argued that the Laves phase that forms within their 441ss-like alloy (theirs contains the addition of Mo) blocks the grain boundary diffusion of Si, limiting the formation of a Si-rich phase in the oxide scale. In general, there are several requirements for grain boundary blocking to be effective:

1. Grain boundary diffusion needs to contribute significantly to the diffusion of the species of interest.
2. The blocking agent needs to reside on the grain boundaries.
3. The blocking agent needs to tie up the excess vacancies found on grain boundaries which are the source of the faster grain boundary diffusion.
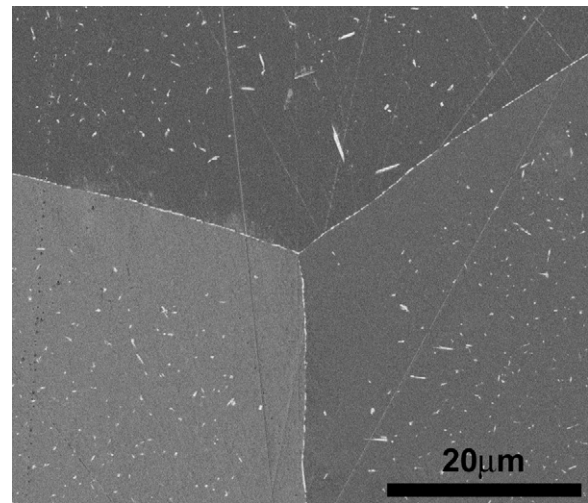

Fig. 12. SEM micrograph of the 441ss − std alloy after solutioning at 1200 °C for 2 h followed by 800 °C for 2 h is shown above. Note that the Laves phase (lighter appearing phase) is found both on the grain boundaries as well as within the grains.

Each of these requirements will be considered in turn to determine their applicability in alloy 441ss. First, it is well established that grain boundary diffusion is a significant contributor to the overall diffusion of substitutional elements within a material up to about 0.5 of T_m, where T_m is the alloy melting temperature in Kelvin. Above this temperature, bulk diffusion through the lattice becomes the dominant contributor to diffusion. For alloy 441ss, 800 °C is approximately 0.6 T_m, therefore, grain boundary diffusion can be expected to play an important role in the diffusion of Si.

With respect to the second requirement, the Laves phase can be found on the grain boundaries, however, no preference for grain boundary precipitation of this phase is observed in our samples (Fig. 12) or in the samples of other researchers [33]. Finally, while having the blocking agent on the boundary is a prerequisite, it is not sufficient to provide effective blocking. In fact, if the grain boundary phase does not tie up excess vacancies within the boundary, it can effectively increase the grain boundary area, thus increasing the contribution from grain boundary diffusion. Sim et al. [40] have considered the coherency of the Laves phase with the matrix in an alloy comparable to alloy 441ss (slightly lower in Cr) and have concluded through high resolution TEM that the Laves phase is not coherent with the matrix. Finally, while Horita et al. [41] report the absence of grain boundary ridges on oxidized surfaces of a Laves phase containing alloy oxidized in moist hydrogen, Yang et al. [33] actually observed grain boundary ridges on specimens of alloy 441ss oxidized in air, which agrees with our observations as well [49]. Furthermore, the lack of grain boundary ridges in the Horita et al. [41] work is inconclusive because no mention of grain size (i.e., ridge spacing) was included. From this body of evidence, we conclude that the Laves phase is unlikely to block grain boundary diffusion of Si in alloy 441ss. Furthermore, even if grain boundary diffusion of Si is completely avoided, bulk diffusion will still be operable, and arguably the dominant contributor, at 800 °C. As a result, over the 40,000 h anticipated lifetime of the interconnect, a significant amount of Si can be anticipated to migrate to the oxide scale.

Yang et al. [33] have proposed that the grain boundary Laves phase "captures" the Si and prevents an insulating Si layer from forming at the scale/metal interface. In Section 3.2 we demonstrated that the Si in the Laves phase can account for only about 0.11 wt.% of the Si in the alloy, leaving 0.23 wt.% remaining in the matrix. A similar application of Eq. (1) to the work of Yang et al. [33] suggests that their alloy 441ss (which contains a nominal Si

content of 0.47 wt.%) will retain about 0.34 wt.% Si in the matrix. Alman and Jablonski [30] have shown that even in a ferritic stainless steel with very low Si (350–530 ppm), Si-rich subscales begin to form after as little as 2300 h at 800 °C. The 441ss – std alloy of this study contains 1.75 vol.% Laves phase at 800 °C. If this phase were to capture all of the Si within the alloy it would contain approximately 18 wt.% Si (34 at.%). Since the Laves phase is an A_2B compound this would mean that at least some of the Si would sit on A sites while the remainder would sit on B sites. In an alloy with slightly higher Si content, such as the one reported on by Yang et al. [33] the Laves phase would need to contain approximately 20 wt.% Si which is nearly 37 at.%. Clearly this is an unlikely scenario. Furthermore, thermodynamics indicate that Si does not form an equilibrium Laves phase with Fe, Nb, Ti or Cr [43–46] the four major constituents of the Laves phase found within alloy 441ss. Thus, sufficiently high matrix Si levels can be expected to result in the formation of a Si-rich subscale during oxidation of alloy 441ss.

The TEM results (Fig. 11) confirm that an amorphous Si-rich layer forms at the scale/metal interface and surrounds some of the chromia grains within 2000 h of exposure at 800 °C. The layer at the metal/oxide interfacial region appears to nucleate and grow from matrix Si and appears to be the same Si-rich layer observed in the SEM (Fig. 10). Once present, the Si-rich scale does not grow rapidly, or perhaps it has an extended nucleation period reaching only ~10 nm in thickness after 2000 h at 800 °C. Nevertheless, it is expected that the ~10 nm thick layers of Si-rich oxide will be quite resistive, since the resistivity of both crystalline silica and amorphous silica is on the order of 10^5–10^7 ohm cm at 800 °C [47], which is substantially higher than that of the Cr–Mn spinel layer (~16 ohm cm at 800 °C [48]). An estimate of the expected area specific resistance (ASR) of a 10 nm layer of silica predicts an ASR of 0.1–10 ohm cm^2 for a 1 cm^2 contact area. This is several orders of magnitude higher than the ASR measured by Yang et al. [33] on either bare or Co–Mn spinel coated alloy 441ss. However, this data is suspect on several accounts: they report an essentially constant ASR for the Co–Mn spinel coated alloy 441ss while they also report a parabolic oxide scale growth rate (albeit reduced in comparison to the uncoated alloy 441ss). These two observations are in conflict. It is unlikely that the interconnect ASR will remain constant over time while the scale thickness grows since it is the scale resistivity that outweighs the other contributions to the resistivity of the interconnect independent of whether a Si-rich oxide subscale forms. Perhaps there are other phenomena occurring during the ASR test, such as further in situ sintering or even short circuit or low resistance paths developing, that produce these conflicting results.

5. Conclusions

The results of this study suggest that the formation of Laves phase in 441ss alloys designed for high temperature fuel cell interconnects may not prevent the formation of a Si-rich layer in the oxide scale. Specifically:

1. The Laves phase does not remove all the Si from the matrix.
2. The Laves phase does not block grain boundary diffusion.
3. Si-rich oxides are formed at the scale/metal interface of alloy 441ss without a Co–Mn spinel coating. Such a coating may act to delay (but not avoid) the formation of Si-rich oxides by slowing the rate of oxidation.
4. Si-rich oxides are more readily formed at the scale/metal interface of the Nb-free (and therefore Laves-free) alloy.
5. It may be that the Si-rich oxide is not continuous in standard 441ss alloys, or is doped so that it is conductive, and thus responsible for the low, long-term ASR reported by others on this

alloy. However, it is more likely that the long-term, low ASR results from a series of complex mitigating factors that occur during testing, since the outer scale continued to grow while the reported ASR remained constant.

The low measured ASR of alloy 441ss remains compelling, however the only way to elucidate the true applicability of this alloy as a SOFC interconnect is to perform long-term tests in situ, as part of an operating SOFC stack.

References

[1] Fuel Cell Handbook, 7th ed., EG&G Technical Services, under Contract Number DE-AM26-99FT40575 with US Dept of Energy, Office of Fossil Energy, National Energy Technology Laboratory, 2004 (Chapter 1).
[2] N.Q. Minh, J. Am. Ceram. Soc. 76 (3) (1993) 563–588.
[3] Fuel Cell Handbook, 7th ed., EG&G Technical Services, under Contract Number DE-AM26-99FT40575 with US Dept of Energy, Office of Fossil Energy, National Energy Technology Laboratory, 2004 (Chapter 7).
[4] M.C. Williams, J.P. Strakey, W.A. Surdoval, J. Power Sources 143 (2005) 101–196.
[5] M.C. Williams, J.P. Strakey, W.A. Surdoval, L.C. Wilson, Solid State Ionics 177 (2006) 2039–2044.
[6] M.C. Williams, J.P. Strakey, W.A. Surdoval, J. Power Sources 159 (2006) 1241–1247.
[7] S. de Souza, S.J. Visco, L.C. De Jonghe, Solid State Ionics 98 (1997) 57.
[8] H. Ishihara, H. Matsuda, Y. Takita, J. Am. Chem. Soc. 116 (1994) 3801.
[9] M. Feng, J.B. Goodenough, Eur. J. Solid State Inorg. Chem. T31 (1994) 663.
[10] P. Huang, A. Petric, J. Electrochem. Soc. 143 (5) (1996) 1644.
[11] K.Q. Huang, R. Tichy, J.B. Goodenough, J. Am. Ceram. Soc. 81 (1998) 2565.
[12] W.Z. Zhu, S.C. Deevi, Mater. Res. Bull. 38 (2003) 957–972.
[13] T. Horita, Y.P. Xiong, K. Yamaji, N. Sakai, H. Yokokawa, J. Power Sources 118 (2003) 35.
[14] Z. Zeng, K. Natesan, Solid State Ionics 167 (2004) 9.
[15] K. Huang, P.Y. Hou, J.B. Goodenough, Solid State Ionics 129 (2000) 237.
[16] J.W. Fergus, Mater. Sci. Eng. A397 (2005) 271.
[17] S. Geng, J. Zhu, J. Power Sources 160 (2006) 1009–1016.
[18] S.J. Geng, J.H. Zhu, Z.G. Lu, Scripta Mater. 55 (2006) 239–242.
[19] S.P. Simner, M.D. Anderson, G.-G. Xia, Z. Yang, L.R. Pederson, J.W. Stevenson, J. Electrochem. Soc. 152 (4) (2005) A740.
[20] M.C. Tucker, H. Kurokawa, C.P. Jacobson, L.C. De Jonghe, S.J. Visco, J. Power Sources 160 (2006) 130.
[21] M. Kumpelt, T. Kaun, T.A. Cruse, M. Hash, in: SECA Annual Workshop, May 11–13, 2004, available at http://www.seca.doe.gov.
[22] S.P.S. Badwal, R. Deller, K. Foger, Y. Ramprakash, J.P. Zhang, Solid State Ionics 99 (1997) 297.
[23] Y. Matsuzaki, I. Yasuda, Solid State Ionics 132 (2000) 271.
[24] S.P. Jiang, J.P. Zhand, X.G. Zheng, J. Eur. Ceram. Soc. 22 (2002) 361.
[25] Z. Yang, G. Xia, P. Singh, J.W. Stevenson, J. Power Sources 155 (2006) 246.
[26] X. Chen, P.Y. Hou, C.P. Jacobson, S.J. Visco, L.C. De Jonghe, Solid State Ionics 176 (2005) 425–433.
[27] Z. Yang, G. Xia, G. Maupin, J. Stevenson, Surf. Coat. Technol. 201 (2006) 4476–4483.
[28] Z. Yang, G. Xia, X. Li, J. Stevenson, Int. J. Hydrogen Energy 32 (2007) 3648–3654.
[29] J. Wu, C.D. Johnson, R.S. Gemmen, X. Liu, J. Power Sources 189 (2009) 1106.
[30] D.E. Alman, P.D. Jablonski, Int. J. Hydrogen Energy 32 (2007) 793.
[31] D. Dulieu, J. Cotton, H. Greiner, K. Honegger, A. Scholten, T. Seguelong, in: P. Stevens (Ed.), Proceedings of Third European SOFC Forum, European Solid Oxide Fuel Cell Forum, Switzerland, 1998, p. 447.
[32] S. Chandra-Ambhorn, Y. Wouters, L. Antoni, F. Toscan, A. Galerie, J. Power Sources 171 (2007) 688.
[33] Z. Yang, G. Xia, C. Wang, Z. Nie, J. Templeton, J. Stevenson, P. Singh, J. Power Sources 183 (2008) 660–667.
[34] Metals Handbook Tenth Edition, V1, Properties and Selection: Irons, Steels and High-Performance Alloys, ASM International, Materials Park, OH, 1990, p. 847.
[35] http://www.alleghenyludlum.com/ludlum/Documents/441.pdf.
[36] T.B. Massalski (Ed.), Fe–Nb Phase Diagram in Binary Alloy Phase Diagrams, 2nd ed., ASM International, Materials Park, OH, 1992, p. 1732.

[37] J. Froitzheim, G.H. Meier, L. Niewolak, P.J. Ennis, H. Hattendorf, L. Singheiser, W.J. Quadakkers, J. Power Sources 178 (2008) 163–173.
[38] N. Fujita, K. Ohmura, A. Yamamoto, Mater. Sci. Eng. A 359 (2003) 272–281.
[39] T.F. de Andrade, A.M. Kliauga, R.L. Plaut, A.F. Padilha, Mater. Charact. 59 (2008) 503–507.
[40] G.M. Sim, J.C. Ahn, S.C. Hong, K.J. Lee, L.S. Lee, Mater. Sci. Eng. A 396 (2005) 159–165.
[41] T. Horita, H. Kishimoto, K. Yamaji, Y. Xiong, N. Sakai, M.E. Brito, H. Yakokawa, J. Power Sources 176 (2008) 54–61.
[42] Jablonski, Cowen, Met. Trans. 40B (2009) 182.
[43] T.B. Massalski (Ed.), Fe–Si phase Diagram in Binary Alloy Phase Diagrams, 2nd ed., ASM International, Materials Park, OH, 1992, p. 1771.
[44] T.B. Massalski (Ed.), Nb–Si Phase Diagram in Binary Alloy Phase Diagrams, 2nd ed., ASM International, Materials Park, OH, 1992, p. 2859.
[45] T.B. Massalski (Ed.), Ti–Si Phase Diagram in Binary Alloy Phase Diagrams, 2nd ed., ASM International, Materials Park, OH, 1992, p. 3367.
[46] T.B. Massalski (Ed.), Cr–Si Phase Diagram in Binary Alloy Phase Diagrams, 2nd ed., ASM International, Materials Park, OH, 1992, p. 1732.
[47] W.D. Kingery, H.K. Bowen, D.R. Uhlmann, Introduction to Ceramics, 2nd ed., Wiley, New York, 1975.
[48] Z.G. Lu, J.H. Zhu, E.A. Payzant, M.P. Paranthaman, J. Am. Ceram. Soc. 88 (4) (2005) 1050–1053.
[49] Jablonski, Cowen, Unpublished Research (2009).